MTOC clustering and nuclear division through proper spindle positioning in yeast: a microtubule grow-and-catch model

Saptarshi Chatterjee,[1,*] Subhendu Som,[1,†]
Neha Varshney ♠,[2,‡] Kaustuv Sanyal,[2,§] and Raja Paul[1,¶]

[1]*Indian Association for the Cultivation of Science, Kolkata -700032, India*

[2]*Molecular Mycology Laboratory, Molecular Biology and Genetics Unit, Jawaharlal Nehru Centre for Advanced Scientific Research, Jakkur, Bangalore -560064, India*

Abstract

Mitotic spindle formation in pathogenic budding yeast, *Cryptococcus neoformans*, depends on multitudes of inter-dependent interactions involving kinetochores (KTs), microtubules (MTs), spindle pole bodies (SPBs) and molecular motors. Before the formation of mitotic spindle, multiple visible microtubule organizing centers (MTOCs), coalesce into a single focus to serve as an SPB. We propose a 'grow-and-catch' model, in which cytoplasmic MTs (cMTs) nucleated by MTOCs grow and catch each other, promote MTOC clustering. Our quantitative modeling identifies multiple redundant mechanisms mediated by cMT-cell cortex interactions and inter-cMT coupling, facilitating MTOC clustering within experimental time frame. Implementing a similar stochastic model in mitotic spindle where MTs 'grow-and-catch' KTs, we further demonstrate that impaired error correction may lead to an asymmetric partitioning of chromosomes between mother and daughter cells. However, either a marginal delay in the MT nucleation from the SPB of daughter bud (dSPB) or an enhanced MT nucleation from the SPB in mother (mSPB) needs to account for asymmetric chromosome segregation. Using an analytical model screen, we predict plausible mechanistic conditions for proper spindle positioning. We find that MT buckling together with dynein pull and cortical push maintains proper spindle localization.

♠Present address: Ludwig Institute for Cancer Research, Department of Cellular and Molecular Medicine, University of California San Diego, La Jolla, CA 92093, USA.

*Electronic address: sspsc6@iacs.res.in

†Electronic address: sspss5@iacs.res.in

‡Electronic address: neha.var15@gmail.com
§Corresponding author: sanyal@jncasr.ac.in
¶Corresponding author: raja.paul@iacs.res.in

Introduction

Spatio-temporal dynamics of organelle-constituents relies primarily on the active organization of microtubules (MTs). MTs are semiflexible polymeric filaments having rapidly polymerizing plus ends and slowly polymerizing minus ends. The growth and shrinkage of MTs are governed by intrinsic dynamic instability parameters [1]. In animal cells, the centrosome is a major MT nucleating center which leads to the formation of a radial MT array [2–4]. However, the radial spanning of MTs in many noncentrosomal MT networks is governed by various membrane organelles such as the Golgi apparatus [2, 5–9]. The cellular structures that harbor the ability to nucleate MTs and organize a radial network are often referred to as Microtubule Organizing Centers (MTOCs) [2, 10].

In the ascomycete budding yeast *Saccharomyces cerevisiae*, spindle pole bodies (SPBs), embedded on the nuclear envelope (NE) are analogous to centrosomes. The SPBs are enriched with distinct $\gamma-$tubulin receptors that organize the cytoplasmic MTs (cMTs) and nuclear MTs (nMTs) [11, 12]. γ-tubulin encoded by *TUB4*, physically interacts with Spc98, Spc97 to form γ-tubulin complexes (γ-TuSCs). Subsequently, the receptors of γ-TuSc, Spc110, and Spc72 localize γtubulin complexes to the SPBs and form a γ-tubulin ring complex (γ-TuRC). This provides SPBs distinct nuclear and cytoplasmic domains indicating that a single MTOC can accommodate nucleation sites for both cMTs and nuclear MTs (nMTs) [2, 10, 13].

In contrast to *S. cerevisiae*, where the SPB being the only MTOC, there are several MTOCs present in the basidiomycete budding yeast *Cryptococcus neoformans* during interphase [14–16] (Figure 1A, S1). MTOCs dynamically move toward each other and eventually cluster together to form the mother SPB (mSPB) before SPB duplication (Figure 1A, S1). In *C. neoformans* self-assembly of MTOCs is orchestrated by MT mediated 'grow-and-catch' (also known as 'search and capture') mechanism [14, 17]. Basic characteristics of the clustering mechanisms are shared across a diverse set of organisms as well as several organelle assemblies (e.g. Golgi assembly and stacking, mitochondrial assembly, multi-centrosomal clustering [18] etc.) and are not necessarily organism specific[8]. The mechanics of the MTOC clustering before the formation of the mSPB in *C. neoformans* remains elusive and deciphering the same experimentally is challenging.

After duplication, SPBs separate from each other to facilitate the formation of the mi-

totic spindle. The plus ends of cMTs interact with the cell cortex via microtubule-associated proteins (MAPs) and molecular motor proteins to drive the local movement, positioning, and migration of the spindle toward the daughter bud. Proper spindle positioning and its alignment ensure equal segregation of the nuclear mass [14, 19]. In budding yeast *Saccharomyces cerevisae*, a specific location for the mitotic division is predetermined even before the formation of the spindle [14, 20]. The spindle positioning within a confined geometry with an underlying spatial symmetry can often be mapped onto a centering problem across biological systems. For example, force transduction via the active force generators at the cell cortex leads to the centering of the spindle in HeLa cells. It is followed by symmetric division where the cortical pull is a key contributor in the force balance landscape [21]. Similar spindle localization at the cell center is also observed in *Caenorhabditis elegans* embryo during early prophase [22]. Interestingly, in basidiomycetous budding yeast *C neoformans* the spindle is formed within the daughter cell marked by the bilateral separation of SPBs. Therefore, before the spindle formation, the nucleus migrates toward the daughter bud from the mother [17, 19]. In *S. cerevisiae*, timely nuclear migration toward the mother-daughter bud neck juncture requires directed force generation toward the daughter bud. This directed movement stems from the interplay between dynein pull on the plus ends of the cMTs at the mother and daughter cortex along with Bim1 mediated bias of the cMTs supported by a MyoV based machinery in the mother cell [19]. Our previous study [17] reveals that there is a differential spatial arrangement of dynein puncta across the mother and the daughter cell cortex in *C. neoformans*. In the daughter cell cortex, we observed a single large condensed dynein patch, whereas in the mother cortex dynein puncta are small and distributed over a larger region. This differential spatial organization indicates that a net directed pull from the daughter cell cortex mediated by concentrated dynein molecules in association with Bim1-bias in the mother overrides the opposing pull from the mother cell cortex leading to a net nuclear migration toward the daughter bud. Moreover, the default distributed spatial arrangement of dynein patches in the mother cortex (unlike the highly condensed localized patch in the daughter) further reduces resultant pulling force from the mother cortex.

The stable positioning of the spindle is a crucial determinant of the faithful nuclear segregation. Our earlier experimental findings suggest that the mitotic spindle stabilizes near the septin ring inside the daughter [17]. This spatial configuration poses a natural question: what are the force balance conditions necessary and sufficient for such localization?

In experiments, it is challenging to quantitatively estimate or tweak forces on the spindle to test the effect of such perturbation on nuclear segregation in *C. neoformans*. Previously, various force balance models have been used to replicate the observed aspects of spindle dynamics [23–26]. In this study, we explored two kinds of theoretical modeling setup: 1. analytical force balance model, 2. coarse-grained agent-based model. These two models not only complement the primary experimental observations of spindle localization in *C. neoformans*, but reasonably corroborates with each other, qualitatively. In other words, the benchmarking of the analytical model is supported by the agent-based model and vice versa.

Earlier studies indicate that the interdigitated nMTs crosslinked via kinesins and other molecular players initiate the formation of spindle architecture where some of the nMTs actively establish contact with all the kinetochores (KTs) via KT-MT grow-and-catch mechanism [23, 27–31]. It is observed that during budding yeast mitosis, the KTs remain in a 'preclustered' configuration [14, 15, 32]. Accurate chromosome segregation during cell division requires the formation of stable amphitelic attachments, connections between individual sister KTs to opposite SPBs by kinetochore MTs (kMTs) [33, 34]. We developed a similar KT-MT grow-and-catch model to delineate important mechanical conditions for chromosomal segregation in *C. neoformans*.

Based on the experimental observations on MTOC clustering at different stages of the cell cycle, we simulated our agent-based MT 'grow-and-catch' ('search and capture') model to study the clustering of MTOCs into an SPB. We also proposed an analytical model of force balance that replicates proper spindle positioning in *C. neoformans*. Using the model, we investigated the stable position of the mitotic spindle under the combination of various MT mediated forces. In the end, we simulated the KT search and capture by nuclear MTs both in the presence and absence of an error correction mechanism which rectifies erroneous syntelic attachments and explored the conditions for unequal chromosomal segregation.

Taken together, we show that several mechanistic processes can facilitate efficient clustering of MTOCs, either independently or in harness with the other and buckling of cytoplasmic MTs is indispensable for proper spindle positioning. Furthermore, the model reasonably reproduces the defects in chromosome segregation generated due to the impaired error correction mechanism in *C. neoformans* and identifies plausible initial conditions for the emergent aneuploidy.

Results

Developing *in silico* modeling framework

Computational Modeling: We consider the spindle dynamics occurring inside cellular confinement mimicking a budded cell. The mother bud size (radius R_M) is fixed whereas the daughter bud (radius r_D) grows with time. Prior to the SPB formation, all the MTOCs (spheres of radii r_{MTOC}) are embedded on NE (non-deforming spherical nucleus of radius r_{nuc}) and nucleate cMTs. At the onset of the simulation, we considered 14 MTOCs (if not mentioned otherwise) [16, 17]. Each MT is modeled as a cylinder of zero thickness with its length regulated by four dynamic instability parameters (Table S1): catastrophe and rescue frequency (f_c, f_r); growth and shrinkage velocity (v_g, v_s). After complete clustering of MTOCs (Figure S1, Figure 1A, 1B), mSPB duplicates and nMTs from both the SPBs grow inside the nuclear volume and catch KTs. Meanwhile, the cMTs that reach the cell cortex, majorly experience instantaneous cortical push ($\vec{F}^{cell-mem}_{push-inst}$), push from the MT buckling ($\vec{F}^{buckle}_{cor}$) and pull due to cortical dynein ($\vec{F}^{dyn}_{cor}$). The cMTs grazing along the NE experience an additional force ($\vec{f}_{overlap}$) at the MT-MT overlap on NE which is proportional to the mean number of minus end-directed motors per unit length (λ_{ovl}) at the overlap. Similarly, forces between KTs and nMTs have been computed (for details, see Material and Methods). The instantaneous positions of all the objects (nucleus, MTOCs, SPBs, KTs) are updated by solving corresponding Stokes equations (Eq. 1-4 in Materials and Methods).

Mathematical Modeling: We formulated a mathematical model to study spindle positioning. We frame the mother and the daughter bud as two intersecting circles of radii R_M and r_D respectively (Table S1). The center of the daughter bud is chosen to be 'd' distance away from the center of the mother. We restrict the spatial movement of the spindle along the line joining the centers, regarded as the axis of symmetry. For simplicity, our analytical model is one-dimensional where all the forces are directed along the axis of symmetry, namely the 'X' axis (Figure S2). The spindle is chosen to be a rigid rod of length $2a$ with two perfectly bioriented SPBs at its two ends lying on the X-axis. We assume that the cMTs from the SPB facing the mother (daughter) cortex namely $SPB(L)$ ($SPB(R)$), interact solely with the mother (daughter) cortex. We further consider that the cMT length distribution is exponential [23, 35]. Next, we derive closed-form expressions for various MT-mediated

forces (instantaneous cortical push, cortical dynein pull, force due to MT buckling) on the spindle due to MT-cell cortex interaction. The sum of all these forces accounts for the total force on the spindle. The net force balance on the spindle (rigid rod constituting $SPB(L)$ and $SPB(R)$) determines the spindle position.

In the analytical model, the strength of dynein-mediated pulling is regulated by λ_{dyn}^{M} (Eq. 7-8 in Materials and Methods) and λ_{dyn}^{D} (Eq. 10-11 in Materials and Methods), cortical pushing by A_M and A_D (Eq. 5 and Eq. 6 in Materials and Methods), average MT length by L_{MT}^{av} (Eq. 5-8, Eq. 10-11, Eq. 13-14 in Materials and Methods). In the numerical simulation, the corresponding model parameters are adjusted according to the values listed in Table S1. In most of the cases, the choice of the parameter values is based on the earlier published reports. However, in a few cases, due to the paucity of exact numbers in the literature, the chosen parameter values are optimized for the current study through sensitivity analysis. Below, we present the model investigations exploring MTOC clustering, spindle positioning and chromosome segregation in *C. neoformans*.

Clustering of MTOCs progresses via redundant pathways

We have shown previously that all KTs cluster to form a punctum in 25 mins [17]. We have also demonstrated that KTs colocalize with MTOCs [15]. However, the time required for MTOC clustering remains unknown. Now, we validated the time required for MTOCs to coalesce into an SPB by calibrating the clustering time since bud initiation (time set to zero), in terms of the budding index (Figure S1A, S1B). We observed that since the bud initiation, the daughter bud grows with time, in a reasonably uniform manner, across cells. As the bud growth rate is roughly conserved throughout the cell population, the budding index can be thought of as an intrinsic 'clock' of a budded cell (Figure S1C). The number of MTOCs in cells having similar budding indices (implying that the cells are at the same cell cycle stage) were counted and were plotted with 'time' (calibrated from the budding index) to estimate the MTOC clustering time (Figure 1A). Although electron microscopy suggested as many as 14-16 MTOCs [16], with a limited resolution we could identify a maximum of 8-10 MTOCs in small budded cells.

First, we investigated the MTOC clustering process via MT driven 'grow-and-catch' ('search and capture') on the NE without the cortical interactions. To begin with, we

determined the time required for all the MTOCs to cluster if cMTs growing out of MTOCs slide along the NE and directly grow and catch the MTOCs. We considered that in the 'direct grow and catch' mechanism (Figure 1B), the MTs contributing to the clustering process are confined to the NE. As the 'searcher' MT tip nucleated from an MTOC grows (grazes) along the NE and 'catches' another MTOC ('target'), the MTOCs move toward each other along the MT connection until they fuse (Figure 1B). The movement of the MTOCs is strictly restricted to the NE. In this context, we assumed a fixed number of grazing cMTs per MTOC (4 cMTs per MTOC). We found that the timescale for complete clustering achieved by this 'direct grow-and-catch' pathway is significantly large surpassing the relevant mitotic timescales. The MTOCs take ~ 1.5 h to cluster entirely, that too, in $\sim$ 10 % of the population only. The MTOCs fail to cluster into a single focus, in the rest of the population even after ~ 4 hr. Thus, it is unlikely to be an 'efficient' pathway for MTOC clustering. However, the possibility that the same pathway may work in combination with other efficient pathways cannot be ruled out.

Next, we introduced antiparallel sliding amongst the grazing cMTs on the NE (inter cMT coupling, Figure 1B). Inward sliding of the overlapping cMTs from two different MTOCs can be steered by crosslinking minus end-directed motors [36]. The crosslinking activity of minus end-directed motors acting at the MT-MT overlap brings the engaged MTOCs towards each other. In the earlier scenario, a 'searcher' MT has to grow and catch another MTOC. However, in the present context, a 'searcher' MT can grow and catch another MT segment so that the negative end-directed motors can crosslink them and initiate antiparallel sliding. Adding the negative end-directed motor crosslinking and sliding on the NE facilitate the timely clustering; clustering of all the MTOCs ($\sim$ 100 %) into a single body happens within $\sim$ 23 min (Figure 1C, Video1). As expected, when the inward force between the MTOCs due to negative ended motors diminishes, the net clustering time increases (Figure 1C).

In several models, it has been shown that cellular processes involving MT mediated 'grow-and-catch' mechanisms are often optimized by the regulation of the number of MTs [37, 38]. In a similar 'search and capture' process, as the MT number increases, the capture time gradually decreases to a threshold timescale followed by a saturation [39]; the scenario implies that upon a stepwise increase in the number of MTs per MTOC, the clustering time is expected to decrease. We further investigated the sensitivity to varying cMT numbers in

a case by case fashion; a. the MT number per MTOC is kept constant upon clustering of two MTOCs, b. adding the MT number upon a fusion of the MTOCs up to a maximum limit to 4 MTs per MTOC and then, c. removing the maximum limit respectively (Figure 1D).

It was demonstrated earlier that MTOCs colocalize with KTs (Cse4) [15, 40]. Thus, we examined what happens to the KT clustering if one or more KTs are attached to the MTOCs at the beginning (Figure 1E). Our model predicted that if more than one KT is attached to an MTOC, the KT clustering process is marginally faster than the MTOCs.

Next, we explore the role of cMT-cell cortex interaction in the clustering process. There are two major cortex-based forces on the cMTs: a. net pull on the MT segments sliding inside the cortex via the cortical dyneins towards the cortex; b. Bim1 mediated force on the cMTs that have a directional preference towards the septin ring (MT-cell cortex interaction, Figure 1B). We found that the exclusive activity of dynein mediated MT- cell cortex interaction leads to nearly complete clustering of the MTOCs but the time estimated (~ 240 min) is way too high (Figure 1F, Video2). However, a decrease in the cortical pull and/or subsequent increase in the Bim1 mediated bias reduces the clustering time scale to $\lesssim 50$ min (Figure 1F, Video3). We find that the dynein mediated pull on the MTOCs via cMTs acts in random directions, whereas the Bim1 mediated bias is always directed towards the septin ring. Thus dynein dominated cortical pull suppresses the effective Bim1-bias and delays the clustering. When dyneins are suppressed, due to Bim1-bias all the MTOCs are drifted towards the septin ring while embedded on the NE and cluster.

The time scales for complete MTOC clustering appears to be similar when, a. MTOCs aggregate due to antiparallel sliding of the grazing MTs on the NE via minus ended motors and b. MTOCs aggregate due to diminished cortical dynein pull concomitantly with enhanced Bim1-bias at the cortex (Figure 1G, Table S2). This highlights an important physical possibility that the clustering mechanisms may be redundant, i.e., the mechanisms either act in liaison or independently.

The complete clustering of MTOCs into a single body marks the formation of the mature mother SPB followed by SPB duplication. Subsequently, the duplicated SPBs separate into a bi-oriented configuration that initiates spindle formation. In our earlier and present studies, it has been shown that the mitotic spindle stabilizes inside the daughter bud close to the septin ring in *C. neoformans* (Figure 2A) [17]. To understand the stable spindle

localization, we propose a simple analytical model, that estimates net force balance on the spindle (See Materials and Methods, Supplementary Information, Figure S2). We considered closed-form expressions for various MT-based forces and examined various possibilities of the spindle localization under the combinatory effect of these forces (Figure 2,S2-S4).

Spindle positioning can be determined from the balance of mechanical forces in the cell

A spindle is constantly acted upon by molecular forces arising from the interactions of its components with the surrounding [14, 17], e.g., cMTs interacting with the cell cortex via dynein generates a pull on the nucleus toward the cell periphery; similarly, cMTs buckling in contact with the cell membrane pushes the nucleus away from the membrane. These interactions are plausible in both mother and daughter cell cortices. Besides, interactions of cMTs with the septin ring and the cortical actin cables generate an effective bias translating the plus ends of the cMTs toward the daughter bud. Since these forces are spatially inhomogeneous and rapidly varying with time, it is logical to ask how the nucleus and the spindle attain steady positions before the chromosomal segregation.

We formulate an analytical template in one dimension that accommodates all key MT-mediated force contributors originating from the mother and daughter cortices acting on the SPBs (Figure S2). The mechanistic force balance landscape emerging from the mathematical model allows us to carry out sensitivity analysis across a wide parameter regime constituting a myriad of forces with different characteristics (e.g. instantaneous pushing and buckling of the cMTs, dynein mediated pulling, etc.). From experiments and agent-based simulation, we observe that the average spindle length is ~ 1.5 μm in wild-type (Figure S3A) and the neck to spindle distance is ~ 1 μm while the spindle is in the daughter bud (Figure S3B). Also, the spindle lies almost parallel to the axis of symmetry (orientation angle ~ 15 degree) joining the centers of mother-daughter bud (Figure S3C).

To test how sensitive is the spindle positioning to the cMT-cortex based forces, we introduced instantaneous push and dynein pull from both the mother and daughter cortex. Then, we varied the dynein density in the daughter cortex, keeping the rest of the parameters fixed at base values denoted in Table S1. If the dynein pull from the daughter cortex is too strong, the spindle collapses onto the daughter cortex. In the other limit, the spindle

collapses onto the mother cortex, when the cortical pull from the mother cortex overpowers the pull from the daughter (Figure 2B). Thus, in the absence of MT buckling, the spindle localizes at the cortex.

Adding the force due to MT buckling (with two other forces: cortical pull and instantaneous push) restores the stable spindle position near the septin ring (Figure 2C-2D). The spindle robustly maintains its position inside the daughter bud, close to the septin ring upon considerable variation in the average cMT length (Figure 2D, Table S3).

We also tested the spindle positioning in the absence and presence of MT buckling exploiting a three-dimensional agent-based computational model (Figure S3D-S3E). We find that a moderate dynein pull is crucial for the spindle to migrate into the daughter. In the absence of MT buckling, the spindle localizes deep inside the daughter cortex for moderate and strong dynein pull from the daughter (Figure S3D). However, with MT buckling turned 'on', the spindle settles inside the daughter bud and stabilizes close to the septin ring. The spindle distance from the septin ring measured in the experiment (Figure S3B) and estimated from the analytical (Figure 2D) and computational models (Figure S3E, fourth bar) reasonably agree with each other. Interesting spindle characteristics predicted by the model are summarized in the Supplementary Information, Figure S4, and Table S3.

Impaired error correction may not lead to unequal chromosome segregation

The lifetime of an MT-KT attachment is closely linked with the inter-KT distance and presence of checkpoint protein kinase. Low tension kinetochore-MT attachments, such as syntelic and monotelic attachments undergo degradation owing to the phosphorylation of kinetochore proteins whereas high tension amphitelic attachments are bioriented and stabilized [41]. In the high tension amphitelic attachments, the bioriented configurations are stretched to the extent that their destabilization is minimized. The low tension non-amphitelic attachments, on the other hand, undergo destabilization as their poorly stretched geometric configurations fall under the influence of phosphorylation gradient of the checkpoint proteins preventing aneuploidy. A natural question is: How important is the correction of erroneous attachments for equal division of chromosomes into mother and daughter cells? What exactly happens in the case of unequal division?

We simulated two scenarios: first, the wild-type scenario where the error correction mech-

anism is present; second, the absence of error correction, mimicking Ipl1 depletion (Figure 3A). In the first scenario, a higher degradation rate of wrong attachments resulted in faster attainment of a stable amphitelic configuration (Figure 3B). As the initial KT-MT attachments are formed by the random events of MT 'grow-and-catch', the end possibilities are either amphitelic or syntelic (Figure 3A). In the presence of error correction, all the attachments become amphitelic (Figure 3C, S5A), whereas, in the absence of error correction, half the attachments remain syntelic (Figure 3C). However, both in the presence and absence of error correction, simulations produce almost equal partitioning of chromosomes into mother and daughter cells, i.e., the average fraction of chromosomes in mother relative to daughter cell is ~ 1 (Figure 3D). Clearly, in a population of cells with no error correction in place, the total number of syntelic errors is equally shared by both the SPBs. Hence, the daughter eventually inherits the same number of chromosomes the mother retains. From this observation, we posit that the accumulation of errors may be necessary, but not a sufficient condition for unequal segregation. The fact that the mother retains more chromosomes in Ipl1 depleted cells [17], may relate to the asymmetric functionality of the SPBs, where the properties of nMT nucleation in mSPB differ from that of dSPB.

Combination of MT nucleation defects with impaired error correction may account for unequal division

Previously, we showed that, upon Ipl1 depletion, the segregated mother-daughter nuclear volume ratio tends to shift toward > 1, unlike the wild-type scenario where an equal nuclear division is observed [17]. Note that the segregated nuclear volume is considered to be proportional to the number of chromosomes. The shift of the ratio toward > 1 upon Ipl1 depletion means that the number of chromosomes is more in the mother compared to the daughter.

To explain the unequal partitioning of chromosomes between the mother and the daughter, we hypothesize that the average number of kinetochore-MT attachments from the SPBs staying in the mother (mSPB) and settling into the daughter (dSPB) may differ. To check that, we explored two plausible scenarios. Firstly, the difference in the number of attachments formed by the mSPB and dSPB may be manifested via a delay in MT nucleation from either of the SPBs. We tested this possibility and our model predicts that a configuration

with a greater number of chromosomes in the mother is feasible when there is a delay in nMT nucleation from the dSPB (Figure 4A). The delay in nMT nucleation from the dSPB enhances the chance of syntelic attachments from the mSPB, associating more chromosomes with the mother.

However, in wild-type cells, since a correction mechanism is present, the initial syntelic attachments made from the mSPB eventually degrade and amphitelic configurations emerge, resulting in an equal partitioning of chromosomes (segregation of the nuclear volume) (Figure 4B). In Ipl1 depleted cells, since the error correction mechanism is compromised, the syntelic attachments from the mSPB survive. Figure 4A shows that as the MT nucleation from the dSPB delayed, the fraction of chromosomes in the mother relative to daughter cell increases accordingly.

Secondly, we considered that the number of nMTs emanating from the mSPB is greater than that from dSPB. During early spindle assembly, the number of KT-MT attachments from an SPB is proportional to the number of nMTs emanating from the SPB. Thus, it is likely that the mSPB will capture more KTs compared to the dSPB. This also promotes an enhanced number of syntelic attachments from the mother. In the absence of error correction, a comparatively greater number of erroneous attachments from the mSPB are preserved. This leads to the retaining of a greater number of chromosomes by the mother (Figure 4C). However, when the error correction is functional, the syntelic attachments degrade and amphitely is rescued (Figure 4D).

Finally, we tested another possibility where the KTs are captured from multiple MTOCs. In a population of cells with defects in MTOC clustering, it may occur that even after the formation and duplication of the SPBs, some partially clustered MT nucleating fragments are 'left out' (i.e. failed to merge with the SPB). The 'left out' MTOCs may take a long time to fuse with the larger cluster committed to forming the SPBs. If these 'left out' MTOC fragments participate in the KT capture via an MT 'grow-and-catch' mechanism, and later cluster with any of the SPBs, chances of an unequal division becomes prominent in the absence of error correction mechanism (Figure S5B). If 'left out' MTOCs have a greater chance to merge with the mSPB, more chromosomes are kept in the mother compared to the daughter. To conclude, the model predicted distributions of the fraction of chromosomes in both wild type (Figure 4E) and Ipl1 depleted cells, assuming delayed MT nucleation from the dSPB (Figure 4F), appear to correlate with the experimental data in a post-anaphase

scenario [17].

Discussion

Our theoretical approach works with a) an agent-based computational model of MT grow-and-catch (search and capture), and b) an analytical model to understand the spindle positioning that is partly supported by an agent-based model as well. With the help of the computational model, we examined the role of MT grow-and-catch (search and capture) in MTOC clustering and partitioning of chromosomes into mother and daughter cells. Using the analytical model, we screen various combinations of the MT-based mechanistic forces and find out plausible mechanical force balance conditions that may orchestrate proper spindle positioning. We reached the following conclusions.

The emergent time scales for MTOC clustering are similar in two scenarios; the design principles of which are based on a) effective inter-MTOC attraction due to minus end-directed motor crosslinking between grazing antiparallel MTs on the NE and b) effective drift of all the MTOCs towards the septin ring due to Bim1 mediated cortical bias with diminished dynein pull at the cortex. In the first scenario, the clustering time scales down with the minus end motor mediated inward force at the MT-MT overlap. In the latter one, the clustering time scales up with the net cortical dynein pull on the MTs. From a model perspective, the comparable timescales of these two independent clustering mechanisms indicate a possible redundancy between two mechanisms.

Our analytical model, by screening various MT-based forces, qualitatively highlights the mechanical requirements for proper spindle positioning. It has been suggested that the plane of mitotic division is defined by this stable positioning of the spindle inside the daughter bud with spindle orientation almost parallel to the axis joining the centers of the mother and daughter buds[14, 17, 42]. Our model shows that in the presence of two opposing forces, instantaneous cortical push and dynein pull (no MT buckling), the spindle collapses onto the cortex. Additional force due to MT buckling at the mother and daughter cortex is essential to restore the stable positioning of the spindle near the septin ring. A key reason is the force due to buckling that scales with the inverse square of the MT length. Thus, when the spindle is close to the cortex, buckling MTs strongly push it away preventing the collapse. The analytical model also shows several interesting positions of the spindle which

are unstable. The one-dimension model, however, can be extended to higher dimensions which would include several important characteristic degrees of freedom (e.g. orientation of the spindle, the angular displacement of the SPBs, etc.) in the analysis as well.

To examine the physical basis and the consistency of the spindle positioning attributes, the analytical model results are compared with an agent-based computational model. One of the basic differences between the analytical and computational models is the stochastic effects. The computational model entails stochastic fluctuations stemming from the MT dynamic instability, a finite number of MTs, motor activity, etc.; whereas the analytical model, for simplicity, does not contain stochastic fluctuations, as well as temporal degrees of freedom. Possibly, due to intrinsic fluctuations in the computational model, we do not observe any unstable spindle position.

For the timely capture of the chromosomes during spindle assembly, an important factor is the directional bias in the MT searching for KTs. In our simulations, the nMTs explore the nuclear volume and search for KTs clustered within. Since the SPBs remain adjacent immediately after the duplication, all the KTs get uniformly exposed to nMTs from both the SPBs. We consider that nMTs start searching for the KTs ('grow-and-catch'/'search and capture') soon after the SPB duplication and examined various pathways for the KT capture: (a) nMTs from the SPBs grow in random directions (Figure S6A), (b) nMT are nucleated toward the KT cluster - accordingly, the nMTs do not explore the complete nuclear volume (Figure S6B), (c) nMTs are prevented from premature catastrophe by the gradient (Figure S6C) or (d) the absolute local concentration of RanGTP like chemical sensed by the growing MT tip directed toward the KT cluster (Figure S6D). These pathways are in qualitative agreement with the previous studies. In fact, in fission yeast, it has been observed that nMTs explore a section of the constrained nuclear volume via pivoted diffusion while searching for the KT [43–45]. Previous computational and experimental studies illustrated the evidence of a similar gradient dependent MT stabilization rendering a higher MT density 'cloud' around the chromosomes [31, 38, 46]. In the present system, it turns out that over a range of nMT-number, the capture time for all the KTs does not vary significantly across the mechanisms explored in the simulation. One possibility for this particular outcome could be the proximity of the SPBs soon after the duplication.

In general, the KT capture via the MT grow-and-catch process leads to four possible configurations of KT-MT attachments [41, 47]. Once the sister KTs are captured by MTs from

opposite SPBs, stable amphitelic attachments are established. When sister KTs are linked to the same SPB, erroneous syntelic attachments are established. If only one sister KT is attached to the pole, monotelic attachments are formed. Another plausible configuration is when both the sister KTs are unattached. The erroneous non-amphitelic kinetochore-MT attachments lead to various defects due to unequal segregation; the ramifications of which are attributed to cancer [41, 48, 49]. The amphitelic attachments may be achieved progressively by two central mechanisms. First, the error-correction mechanism that detects and destabilizes the incorrect kinetochore-MT attachments, thereby giving cells a chance to achieve biorientation. Second, the spindle assembly checkpoint (SAC) senses the attachment state of the KTs and delays the anaphase onset until amphitely is achieved. Previous studies report that the error-correction mechanism in budding yeast is governed by the Aurora B kinase homolog Ipl1 where erroneous kinetochore-MT attachments (e.g. low tension syntelic attachments) are degraded via Ipl1 mediated phosphorylation of individual kinetochore proteins. The high-tension bioriented amphitelic attachments stays out of Ipl1 phosphorylation cloud and remain stable [41, 50–54]. In absence of Ipl1-mediated phosphorylation gradient, abundant stable syntelic attachments are established in Ipl1 depleted cells.

Our model outcome justifies that an impaired error correction mechanism alone may not be responsible for the unequal partitioning of the chromosomes between mother and daughter cells. For unequal segregation, the erroneous attachments must be unequally shared between the mother and the daughter SPBs. This may occur when the MT nucleation/stabilization from either the mother or the daughter SPB is impaired. Earlier experiments in *C. neoformans* [17] show that the mother cell retains more chromosomes compared to the daughter cell upon Ipl1 depletion. Our simulations indicate that impaired MT nucleation from the dSPB may contribute to the accumulation of a greater number of chromosomes in the mother. Several studies refer asymmetric functionality of the SPBs (such as maturation delay between the two SPBs [55–57]) leading to the difference in the MT number [58, 59].

In the current study, we constructed a phenomenology based model that consistently explores various aspects of spindle assembly during mitotic cell division. Using the model, we have been able to elucidate several important features of MTOC clustering, spindle positioning, and chromosomal segregation, largely from a mechanistic point of view. However, the attributes of the dynamic processes involved in the mitotic cell cycle differ widely across different cell types. Different organisms evolved (with increasing complexity at the molec-

ular level) to self-engineer the process of cell division. Thus, investigating the mechanistic principles of the cell division across different organisms using a systems biology-based approach in collaboration with molecular biology experiments stands as the subject of future research.

Materials and Methods

Media and growth conditions

The conditional mutant strains harboring the GAL7 promoter were grown in YPG (1 % yeast extract, 2 % peptone, 2 % galactose) as a permissive medium and YPD (1 % yeast extract, 2 % peptone, 2 % dextrose) as a non-permissive medium at 30° C. The wild-type and deletion mutant strains were grown in YPD at 30° C.

Microscopic image acquisition and processing

The conditional mutant strain CNNV104 was grown till OD600=1 in the permissive medium and re-inoculated in the non-permissive media for 8 h to deplete the subcellular protein. The wild-type strains CNVY107 and CNVY177 were grown in YPD and YPG, respectively overnight. The cells were washed once with 1x phosphate-buffered saline (PBS)to form a suspension. The cell suspension was placed on an agarose (2%) patch present on the slide which was covered by a coverslip. The images were acquired at room temperature using laser scanning inverted confocal microscope LSM 880-Airyscan (ZEISS, Plan Apochromat 63x, NA oil 1.4) equipped with highly sensitive photo-detectors or Axio Observer Calibri (ZEISS). The Z- stack images were taken at every 0.5 μm and processed using ZEISS Zen software/ImageJ. All the images were displayed after the maximum intensity projection of images at each time using ImageJ.

Post-acquisition analysis

The budding indices of cells were calculated as the ratio of the diameter of the daughter cell to the diameter of the mother cell. The diameters were measured by drawing a straight line using a line tool in ImageJ.

Simulation Procedure

Modeling the cellular confinement

The geometric construction of the whole cell is considered to be the intersection of two unequal spheres representing the mother bud (radius R_M) and the daughter bud (radius r_D). The septin ring is marked by the circle spanned at the intersection of the two spheres. The mother bud volume remains constant, while the growth rate of the daughter bud is tuned taking a cue from the experimental observations. The nucleus is taken as a sphere (radius r_{nuc}). Underneath the cell boundary, a cortical layer of finite width l_c accounts for the MT interaction at the cortex. The characteristic parameters (e.g. dynein density etc.) of the cortical layer at the mother bud and the daughter bud are controlled independently due to possible functional differences at the molecular level [14, 17].

Modeling the MTs

MTs are modelled as semiflexible polymers characterized by four innate dynamic instability parameters, viz, growth velocity (v_g), shrinkage velocity (v_s), catastrophe frequency (f_c) and rescue frequency (f_r). While probing for an alternative mechanism, f_c of the MTs searching for the KT is modulated by the local concentration/gradient of the RanGTP like chemical. MTs hitting the cortex experience dynein pull, undergo buckling transition when pivoted and apply an instantaneous pushing force on the nucleus. A subpopulation of MTs, graze along the cortex and the NE.

Modeling MTOCs and kinetochores

The KTs and MTOCs are modeled similarly as done in the previous studies [14, 17]. MTOCs are rigid spheres embedded on the NE and the movement of the MTOCs is strictly confined to the NE. SPBs also considered as rigid spheres (radius r_{SPB}) and embedded on the nuclear envelop.

Spherical KTs with a hard-core repulsion ($\vec{f}_{intersection}$) prevent any finite overlap amongst the KTs. The repulsive force is proportional to the instantaneous overlap between two overlapping KTs [17]. Sister KTs remain paired with each other by the cohesin spring until

metaphase. A Hookean force, proportional to the inter-KT separation, is introduced amongst the sister KTs to account for the effect of the cohesin spring holding them together [14, 17]. In the computational model, the Hookean force is given by $\vec{f}_{cohesin} = K_{cohesin}\vec{d}_{KT-KT}$, where $K_{cohesin}$ is the spring constant and $|\vec{d}_{KT-KT}|$ is the instantaneous separation between two sister KTs. Relevant model parameters are listed in Table S1. The description of various MT mediated force interactions is discussed in the following sections and summarized in Table S4.

Modeling cMT-cell cortex interaction and the inter cMT coupling at the NE

From the MTOCs and later from the SPBs, the cMTs nucleate in any random direction within the cell, excluding the nucleus. Various force transductions due to cMT-cell cortex interaction in the *in silico* model construction are categorically listed in the following.

1. When a growing cMT reaches to the cortex and hits the cell boundary, the steric cell boundary impedes the MT tip against its growth. We characterize the instantaneous force exerted on the MT tip upon each encounter with the cell boundary as an instantaneous push ($\vec{f}^{cell-mem}_{push-inst}$). The magnitude of the instantaneous push is taken to be 1 pN per MT on each encounter. The net instantaneous push is $\vec{F}^{cell-mem}_{push-inst}= \sum_{cMTs} \vec{f}^{cell-mem}_{push-inst}$.

2. Apart from the instantaneous push, a MT growing inside the cell cortex undergoes sliding. The 'bent' sliding segment inside the cell cortex provides anchorage points for the cortical dyneins. For computational simplicity, we introduce the parameter, mean number of dyneins per unit length in mother (daughter) cortex ($\lambda^{M(D)}_{dyn}$) on the MT segments inside the cortex. The force due to the dynein pull on a cMT ($\vec{f}^{cor}_{dyn}$) is proportional to $\lambda^{M(D)}_{dyn} l_{cor}$, where l_{cor} is the combined length of the penetrated MT segment inside the cell cortex. M, D in the suffix denotes mother and daughter cell cortex respectively. The net cortical dynein pull is $\vec{F}^{cor}_{dyn}=\sum_{cMTs} \vec{f}^{cor}_{dyn}=\sum_{cMTs} \lambda^{M(D)}_{dyn} l_{cor}\ \vec{f}_{dyn}$, where $\vec{f}_{dyn}$ is the force generated by a single dynein motor.

3. Similarly, the force due to Bim1 bias on a cMT within mother cortex is $\vec{F}^{cor}_{Bim1}=\sum_{cMTs} \vec{f}^{cor}_{Bim1}=\sum_{cMTs} \lambda^{M}_{Bim1} l_{cor}\ \vec{f}_{Bim1}$ where $\vec{f}_{Bim1}$ is the force generated by a single Bim1 motor. The force due to Bim1 is directed toward the septin ring (Table S4). In the daughter cortex, there is no Bim1 bias. For simplicity, we chose $\lambda^{M}_{Bim1}=\lambda^{M}_{dyn}$.

4. The MTs impinged at the cell membrane also undergo buckling transition (we considered

first-order Euler buckling in the present context). Whether a MT hitting the cell membrane, deep inside the cortex, will transduce dynein mediated pull or a net push away from the cortex due to Euler buckling or undergo catastrophe is dictated by predefined probabilities $P_{buckle}^{cell-mem}$, $P_{dyn-pull}^{cell-mem}$ and $P_{cat}^{cell-mem}$, where $P_{buckle}^{cell-mem}$ = 1- $P_{dyn-pull}^{cell-mem}$-$P_{cat}^{cell-mem}$. The buckling force ($\vec{f}_{buckle}^{cor}$) is proportional to l^{-2} where l is the concerned cMT length. The net buckling force is $\vec{F}_{buckle}^{cor}$= $\sum_{cMTs} \vec{f}_{buckle}^{cor}$ ($|\vec{f}_{buckle}^{cor}|$=Dl^{-2}, where D refers to the flexural rigidity of the MT $\sim$ 200 pN μm^2). In mother cortex, $P_{dyn-pull}^{cell-mem}$=0.0, $P_{buckle}^{cell-mem}$=0.5, $P_{cat}^{cell-mem}$=0.5; in daughter cortex, $P_{dyn-pull}^{cell-mem}$=0.8, $P_{buckle}^{cell-mem}$=0.1, $P_{cat}^{cell-mem}$=0.1.

5. Moreover, a polymerizing MT at the cortex experiences resistance from the cortex on the MT tip in the vicinity of the cell membrane. The force exerted on the MT tip due to this resistance is chosen to be Hookean spring-like. We estimate the force on a polymerizing MT ($f_{cor}^{MT-poly}$) deep inside the cortex as $k_{cor}l_{cor}$. Here, k_{cor} is the equivalent spring constant characterizing $f_{cor}^{MT-poly}$ that pushes the MT tip away from the cortex. We evaluate the net push on the MTOCs/SPBs due to MT polymerization inside the cortex ($F_{cor}^{MT-poly}$) by summing the force contributions ($f_{cor}^{MT-poly}$) overall growing MTs within the cortical region ($F_{cor}^{MT-poly}$=$\sum_{MTs}^{cortex} f_{cor}^{MT-poly}$).

To estimate the force due to the inter cMT coupling at the NE $\vec{f}_{overlap}$, we evaluate the net overlap length (l_{ovl}) between a pair of overlapping antiparallel MTs. The force exerted on the MTOCs is proportional to $\lambda_{ovl}l_{ovl}$, where λ_{ovl} is the mean number of minus end-directed motors per unit length at the MT-MT overlap on the NE.

Modeling nMT-kinetochore interaction

The nMTs are categorized into two distinct subsets, interdigitated MTs within the nuclear volume facilitating biorientation of SPBs via molecular motors i.e. interpolar MTs (ipMTs) and MTs establishing contact between SPBs and KTs i.e. kinetochore MTs (kMTs). The collective activity of crossbridging kinesin-5 motors at the ipMT-ipMT overlaps generates a force $f_{ipMT} = l_{ovl}^{ipMT}\lambda_{ipMT}f_{kinesin-5}$ where l_{ovl}^{ipMT} is the total overlapping length summed over all ipMTs emanating from two SPBs. λ_{ipMT} is the average number of kinesin-5 motors per unit length at the ipMT-ipMT overlap. $f_{kinesin-5}$ is the force exerted by a single kinesin-5 motor.

Stochastic growth and shrinkage of the kMTs due to dynamic instability leads to a tug

of war between several oppositely directed competing forces. During the growth phase of the kMT, the kMT tip imparts a net push $f_{push}^{growth} = l_{pen}K_{fibril}$ on the KT attached to it. Here, l_{pen} is penetration length of the kMT into the KT, K_{fibril} is the stiffness constant of the connecting spring that mimics the KT fibril in the model. A kMT in shrinkage phase, pulls the KT with a force $f_{pull}^{shrinkage} = l_{separation}K_c$, where $l_{separation}$ is the distance between the kMT tip and the corresponding KT. K_c denotes the stiffness constant of the Hookean spring linking the depolymerizing kMT tip and the KT.

To maintain a constant gap between the SPBs and the KT cluster, a length-dependent catastrophe of the kMTs has been incorporated in the model. The catastrophe frequency of a kMT (f_c) is regulated in the following manner, $f_c = hl_{kMT}$, where l_{kMT} is the kMT length [14, 17].

Equations of motions governing the spatiotemporal dynamics of the nucleus, MTOCs, kinetochores, SPBs

Forces due to single cMT interacting with the cortex, are applied on the nucleus and the MTOCs/SPBs, simultaneously. Additionally, the force stemming from the ipMT interaction is also exerted on the SPBs. If $\vec{F}_{nucleus}$, $\vec{F}_{MTOC}$ and $\vec{F}_{SPB}$ are the net resultant forces exerted on the nucleus, MTOC and SPB respectively, the corresponding equations of motion can be gleaned as,

$$\frac{d\vec{R}_{nucleus}}{dt} = \frac{\vec{F}_{nucleus}}{\zeta_{nucleus}} \tag{1}$$

$$\frac{d\vec{R}_{MTOC}}{dt} = \frac{\vec{F}_{MTOC}}{\zeta_{MTOC}} \tag{2}$$

$$\frac{d\vec{R}_{SPB}}{dt} = \frac{\vec{F}_{SPB}}{\zeta_{SPB}} \tag{3}$$

where $\vec{R}_{nucleus}$, $\vec{R}_{MTOC}$ and $\vec{R}_{SPB}$ denote the instantaneous positions of the nucleus, MTOCs and SPBs respectively, at a certain time step. $\zeta_{nucleus}$, ζ_{MTOC}, ζ_{SPB} represent viscous drag on the corresponding objects. $\vec{F}_{nucleus}$, $\vec{F}_{MTOC}$ and $\vec{F}_{SPB}$ contain vectorial contributions from $\vec{F}_{cor}^{MT-poly}$, $\vec{F}_{push-inst}^{cell-mem}$, $\vec{F}_{dyn}^{cor}$ and $\vec{F}_{buckle}^{cor}$.

In a similar fashion, the motion of a KT is dictated by the following equation of motion,

$$\frac{d\vec{R}_{kinetochore}}{dt} = \frac{\vec{F}_{kinetochore}}{\zeta_{kinetochore}} \tag{4}$$

Here, $\vec{R}_{kinetochore}$, $\vec{F}_{kinetochore}$ and $\vec{\zeta}_{kinetochore}$ represent instantaneous position, net force on the KT and the viscous drag experienced by the KT respectively. $\vec{F}_{kinetochore}$ entails a vectorial summation over $\vec{f}^{growth}_{push}$, $\vec{f}^{shrinkage}_{pull}$, $\vec{f}_{ipMT}$, $\vec{f}_{cohesin}$ and $\vec{f}_{intersection}$.

The equations of motion are discretized and solved using Euler's method at every time step.

Mathematical model for spindle positioning in budding yeast

In 2-dimensions we consider that the mother and the daughter bud constitute two intersecting circles of radii R_M and r_D respectively. The axis of symmetry of the cellular confinement (e.g. the mother-daughter conglomerate) is taken to be the X-axis with the origin 'O' at the center of the mother bud. The center of the daughter bud is placed at a distance 'd' from the center of the mother (Figure S2A). We compute various MT-based forces on the spindle upon MT interaction with the cell cortex. The mathematical formulation of various force balance terms (e.g. forces originating from MT pushing, dynein mediated pull on the MTs at the cell cortex, MT buckling, etc.) is characterized by exponential length distribution of MTs [23, 35]. The direction of the forces is depicted in Figure S2B.

Pushing forces

MTs are nucleated from the two SPBs separated by a distance of $2a$ (spindle length) with spindle-center at x. For convenience, we mark the SPB located at the left of the spindle ($SPB(L)$) and the SPB located at the right of the spindle ($SPB(R)$). When an MT nucleates out of the $SPB(L)$, it grows a distance $R_M + x - a$ to establish contact with the cell membrane (Figure S2A). Hence, the instantaneous pushing force on the $SPB(L)$ due to the microtubules hitting the mother cell membrane reads,

$$F^{cell-mem(M)}_{push-inst} = A_M e^{-(R_M+x-a)/L^{av}_{MT}} \tag{5}$$

The exponential weight factor enters the expression due to the length of dynamic MTs governed by the following distribution: $N(l) \propto e^{-l/L_{MT}^{av}}$ where l is the length of the MT under consideration. The instantaneous pushing force from the MTs nucleating out of the $SPB(R)$ have to elongate up to a distance $d+r_D-x-a$ along the axis of symmetry to make a contact with the cell membrane in the daughter bud. Hence, the instantaneous pushing force contribution from the daughter bud cell membrane is,

$$F_{push-inst}^{cell-mem(D)} = A_D e^{-(d+r_D-x-a)/L_{MT}^{av}} \tag{6}$$

Here A_M and A_D define the amplitude of the instantaneous pushing force contribution from the mother and the daughter cell membrane. The prefactors A_M and A_D are proportional to the number of MTs interacting with the cell membrane where instantaneous pushing force per MT is taken to be ~ 1 pN.

Pulling forces

When a MT emanating from the $SPB(L)$ grows all the way to penetrate the mother cortex, the dyneins localized at the cortex anchor to the MT segment orchestrating a net pull ($F_{dyn}^{cor(M)}$) toward the mother cortex. Since an elongating MT segment inside the cortex can bend and undergoes sliding as illustrated in the schematic diagram, the pulling force is categorized into two parts: 1. the pull on the uncurled/straight MT segment in the cortex and 2. the pull on the MT segment engaged in 'lateral sliding' along the cortex. Similarly, MTs nucleating out of the $SPB(R)$ upon elongating up to the daughter cortex can penetrate and experience dynein mediated pull. For a MT nucleating from the $SPB(L)$ within the one-dimensional confinement, it has to extend at least up to a distance of $R_M - l_c + x - a$ to establish a physical contact with the mother cortex. It is also evident from the schematic diagram that after reaching the cortex the 'uncurled' MT tip can advance up to $R_M + x - a$ without bending (Figure S2). Henceforth the net pull on the $SPB(L)$ from the 'uncurled' MT segments in the mother cortex can be evaluated in the following manner.

$$\begin{aligned} F_{dyn(uncurled)}^{cor(M)} &= B_M \lambda_{dyn}^M \int_{R_M-l_c+x-a}^{R_M+x-a} e^{-(s+x-a)/L_{MT}^{av}} ds \\ &= B_M \lambda_{dyn}^M L_{MT}^{av} (e^{l_c/L_{MT}^{av}} - 1) e^{-(R_M+2x-2a)/L_{MT}^{av}} \end{aligned} \tag{7}$$

In a similar manner, we can also evaluate the net dynein pull contribution from the 'arc' like MT segment sliding within the mother cortex. Therefore, the net force due to the dynein

pull on the sliding 'arc' $F^{cor(M)}_{dyn(sliding)}$ reads

$$\begin{aligned} F^{cor(M)}_{dyn(sliding)} &= B_M \lambda^M_{dyn} \int_0^{l^M_{arc}} ds\ e^{-(R_M+x-a+s)/L^{av}_{MT}} \\ &= B_M \lambda^M_{dyn} L^{av}_{MT} e^{-(R_M+x-a)/L^{av}_{MT}} (1 - e^{-l^M_{arc}/L^{av}_{MT}}) \end{aligned} \tag{8}$$

Here l^M_{arc} is the 'arc' like segment traced from the intersection of the axis of symmetry and the mother cell membrane to the peripheral contact of the septin ring with the mother cell membrane. Here for the sake of simplicity, we assume that the sliding MTs passing through the mother cortex extend up to the septin ring. The value of l^M_{arc} is estimated to be

$$l^M_{arc} = \frac{\pi R_M}{2} + R_M \tan^{-1}(x_{sp}/y_{sp}) \tag{9}$$

From $SPB(R)$ we assume that the MTs nucleate in the direction of the daughter bud and interact with the daughter cortex and orchestrate a pull ($F^{cor(D)}_{dyn}$) in a similar fashion with which MTs from $SPB(L)$ interact with the mother cortex. Thus, the net pull due to the anchored dyneins on the 'uncurled' MT segments inside the daughter cortex reads,

$$\begin{aligned} F^{cor(D)}_{dyn(uncurled)} &= B_D \lambda^D_{dyn} \int_{d+r_D-l_c-(x+a)}^{d+r_D-(x+a)} ds\ e^{-(d+s-x-a)/L^{av}_{MT}} \\ &= B_D \lambda^D_{dyn} L^{av}_{MT} (e^{l_c/L^{av}_{MT}} - 1) e^{-(2d-2x-2a+r_D)/L^{av}_{MT}} \end{aligned} \tag{10}$$

Similarly, we can compute the contribution in the net dynein pull on $SPB(R)$ from the 'sliding arc' passing through the daughter cortex in the following manner.

$$\begin{aligned} F^{cor(D)}_{dyn(sliding)} &= B_D \lambda^D_{dyn} \int_0^{l^D_{arc}} ds\ e^{-(d+r_D-x-a+s)/L^{av}_{MT}} \\ &= B_D \lambda^D_{dyn} L^{av}_{MT} e^{-(d+r_D-x-a)/L^{av}_{MT}} (1 - e^{-l^D_{arc}/L^{av}_{MT}}) \end{aligned} \tag{11}$$

Here, l^D_{arc} is estimated to be the arc length traced from the intersection of the axis of symmetry with the daughter cortex and the peripheral contact of the septin ring with the cell membrane. From the schematic diagram we obtain the l^D_{arc} to be

$$l^D_{arc} = \frac{\pi r_D}{2} + r_D \tan^{-1}\left(\frac{d - x_{sp}}{y_{sp}}\right) \tag{12}$$

Note here that the prefactors B_M and B_D are proportional to the number of MTs experiencing dynein mediated pulling in the mother and the daughter cortex respectively.

In the above analysis, we have assumed that the effective dynein density is smeared uniformly across the whole mother and daughter cortex. However, experimental observations

point toward a non-uniform, differential spatial arrangement of dyneins in the mother and the daughter cortex. These observations prompted us to accommodate the differential spatial profiling of dynein in the mother and the daughter cortex into the current mathematical model. Force transduction due to the differential spatial organization of dyneins in the mother and daughter cortex is described in detail in the Supplementary Information.

Buckling forces

MTs with tips passed into the mother(daughter) cortex can buckle where the buckling probability is a tunable parameter in the current model. MTs impinged and pivoting at the mother(daughter) cortex generate a length-dependent 'pushing' force that increases with the squared inverse length of the MT while undergoing buckling. It is evident from the geometric construction that the forces stemming from MT buckling at the mother and daughter cortex are oppositely directed (Figure S2). We have taken the following form for the force produced by cortical buckling at the mother cortex ($F_{buckle}^{cor(M)}$)

$$F_{buckle}^{cor(M)} = -\frac{D_M}{(R_M + x - a)^2}\ e^{-(R_M+x-a)/L_{MT}^{av}} \tag{13}$$

Similarly, force generated due to the buckling at the daughter cortex $F_{buckle}^{cor(D)}$ is taken as

$$F_{buckle}^{cor(D)} = -\frac{D_D}{(d + r_D - x - a)^2}\ e^{-(d+r_D-x-a)/L_{MT}^{av}} \tag{14}$$

D_M and D_D are the average number of MTs undergoing buckling transition in the mother and daughter cortices, respectively.

Acknowledgments

This work was supported by the fellowship from SERB (Science and Engineering Research Board), Department of Science and Technology (DST), India (EMR/2017/001346) to RP and Tata Innovation Fellowship (BT/HRD/35/01/03/2017) to KS. SC was supported by fellowship from the University Grants Commission (UGC), India, SS was supported by the fellowship from INSPIRE (IF131156) program DST, India, and NV was supported by the fellowships (09/733 (0253)/219-EMR-I) and 9/733 (0161)/2011-EMR-I from Council of Scientific & Industrial Research (CSIR), India.

[1] M. Dogterom and S. Leibler, Physical Review Letters **70(9)**, 1347 (1993).

[2] J. Wu and A. Akhmanova, Annu. Rev. Cell Dev. Biol. **33**, 4.14.25 (2017).

[3] M. Bornens, Science **335**, 42226 (2012).

[4] P. T. Conduit, A. Wainman, and J. W. Raff, Nat. Rev. Mol. Cell Biol. **16**, 611 (2015).

[5] V. Rodionov, E. Nadezhdina, and G. Borisy, PNAS **96**, 11520 (1999).

[6] K. Chabin-Brion, J. Marceiller, F. Perez, C. Settegrana, A. Drechou, G. Durand, and C. Poüs, Mol. Biol. Cell **12**, 204760 (2001).

[7] L. Hurtado, C. Caballero, M. P. Gavilan, J. Cardenas, M. Bornens, and R. M. Rios, Journal of Cell Biology **193**, 91733 (2011).

[8] T. Vinogradova, R. Paul, A. D. Grimaldi, J. Loncarek, P. M. Miller, D. Yampolsky, V. Magidson, A. Khodjakov, A. Mogilner, and I. Kaverina, Mol. Biol. Cell **23**, 82033 (2012).

[9] T. Vinogradova, P. M. Miller, and I. Kaverina, Cell Cycle **8**, 2168 (2009).

[10] J. Paz and J. Lüders, Trends in Cell Biology **28(3)**, 176 (2018).

[11] J. V. Kilmartin, Philos Trans R Soc Lond B Biol Sci. **369**, 20130456 (2014).

[12] T. chen Lin, A. Neuner, and E. Schiebel, Trends Cell Biol. **25**, 296307 (2014).

[13] T. chen Lin, A. Neuner, Y. T. Schlosser, A. N. Scharf, L. Weber, and E. Schiebel, Elife **3**, e02208 (2014).

[14] S. Sutradhar, V. Yadav, S. Sridhar, L. Sreekumar, D. Bhattacharyya, S. K. Ghosh, R. Paul, and K. Sanyal, Molecular Biology of the Cell **26**, 3954 (2015).

[15] V. Yadav and K. Sanyal, mSphere **3(4)**, e00190 (2018).

[16] M. Yamaguchi, S. K. Biswas, Y. Kuwabara, M. Ohkusu, M. Shimizu, and K. Takeo, Journal of Electron Microscopy **59(2)**, 165 (2010).

[17] N. Varshney, S. Som, S. Chatterjee, S. Sridhar, D. Bhattacharyya, R. Paul, and K. Sanyal, PLoS Genet **15(2)**, e1007959 (2019).

[18] S. Chatterjee, A. Sarkar, J. Zhu, A. Khodjakov, A. Mogilner, and R. Paul, bioRxiv , http://dx.doi.org/10.1101/2019.12.17.879817 (2019).

[19] F. J. McNally, J. Cell Biol. **200(2)**, 131 (2013).

[20] C. G. Rasmussen, J. A. Humphries, and L. G. Smith, Annual Review of Plant Biology **62**, 387 (2011).

[21] T. Kiyomitsu and I. M. Cheeseman, Nat. Cell Biol. **14**, 311 (2012).

[22] D. H. Park and L. S.Rose, Dev. Biol. **315**, 42 (2008).

[23] N. P. Ferenz, R. Paul, C. Fagerstrom, A. Mogilner, and P. Wadsworth, Curr Biol. **19(21)**, 18331838 (2009).

[24] F. Nedelec, J Cell Biol **158**, 1005 (2002).

[25] R. Wollman, G. Civelekoglu-Scholey, J. M. Scholey, and A. Mogilner, Mol Syst Biol **4**, 195 (2008).

[26] B. Rubinstein, K. Larripa, P. Sommi, and A. Mogilner, Phys Biol **6**, 016005 (2009).

[27] M. Kirschner and T. Mitchison, Cell **45**, 329 (1986).

[28] M. Winey and K. Bloom, Genetics **190(4)**, 11971224 (2012).

[29] R. Paul, R. Wollman, W. T. Silkworth, I. K. Nardi, D. Cimini, and A. Mogilner, PNAS **106(37)**, 15708 15713 (2009).

[30] V. Magidson, C. B. O. Connell, J. Lončarek, R. Paul, A. Mogilner, and A. Khodjakov, Cell **146**, 555 (2011).

[31] V. Magidson, R. Paul, N. Yang, J. G. Ault, C. B. OConnell, I. Tikhonenko, B. F. McEwen, A. Mogilner, and A. Khodjakov, Nature Cell Biology **17**, 11341144 (2015).

[32] M. Anderson, J. Haase, E. Yeh, and K. Bloom, Mol Biol Cell **20**, 4131 (2009).

[33] C. E. Walczak, S. Cai, and A. Khodjakov, Nat Rev Mol Cell Biol. **11(2)**, 91 (2010).

[34] R. Heald and A. Khodjakov, J. Cell Biol. **211(6)**, 1103 (2015).

[35] S. Som, S. Chatterjee, and R. Paul, Phys. Rev. E **99**, 012409 (2019).

[36] L. Winters, I. Ban, M. Prelogovic, I. Kalinina, N. Pavin, and I. M. Tolic, BMC Biology , 10.1186/s12915 (2019).

[37] Z. Bertalan, Z. Budrikis, C. A. M. L. Porta, and S. Zapperi, PLOS ONE , 10.1371/journal.pone.0141305 (2015).

[38] R. Wollman, E. Cytrynbaum, J. Jones, T. Meyer, J. Scholey, and A. Mogilner, Current Biology **15**, 828832 (2005).

[39] A. Sarkar, H. Rieger, and R. Paul, Biophysical Journal **116**, 20792091 (2019).

[40] L. Kozubowski, V. Yadav, G. Chatterjee, S. Sridhar, M. Yamaguchi, S. Kawamoto, I. Bose, J. Heitman, and K. Sanyal, mBio **4(5)**, 00614 (2013).

[41] E. S. Tubman, S. Biggins, and D. J. Odde, Cell Systems **4**, 645 (2017).

[42] M. K. Balasubramanian, E. Bi, and M. Glotzer, Current Biology **14**, R806R818 (2004).

[43] I. Kalinina, A. Nandi, P. Delivani, M. R. Chacón, A. H. Klemm, D. Ramunno-Johnson, A. Krull, B. Lindner, N. Pavin, and I. M. Tolić-Nørrelykke, Nat Cell Biol. **15(1)**, 82 (2013).

[44] A. R. Lamson, C. J. Edelmaier, M. A. Glaser, and M. D. Betterton, Biophysical Journal **116**, 1719 (2019).

[45] I. Nayak, D. Das, and A. Nandi, bioRxiv , http://dx.doi.org/10.1101/673723 (2019).

[46] D. J. Odde, Current Biology **15(9)**, R328 (2005).

[47] M. Winey, C. L. Mamay, E. T. O'Toole, D. N. Mastronarde, T. H. Giddings, K. L. McDonald, and J. R. McIntosh, The Journal of Cell Biology **129(6)**, 1601 (1995).

[48] G. J. P. L. Kops, B. A. A. Weaver, and D. W. Cleveland, Nature Reviews Cancer **5**, 773785 (2005).

[49] H. Rajagopalan and C. Lengauer, Nature **432**, 338 (2004).

[50] S. Biggins and A. W. Murray, Genes Dev. **15(23)**, 3118 (2001).

[51] S. Biggins, F. F. Severin, N. Bhalla, I. Sassoon, A. A. Hyman, and A. W. Murray, Genes Dev. **13**, 532 (1999).

[52] I. M.Cheeseman, S. Anderson, M. Jwa, E. M.Green, J. Kang, J. R.Yates, C. S.M.Chan, D. G. Drubin, and G. Barnes, Cell **111(2)**, 163 (2002).

[53] H. Dewar, K. Tanaka, K. Nasmyth, and T. U. Tanaka, Nature **428**, 93 (2004).

[54] T. U.Tanaka, N. Rachidi, C. Janke, G. Pereira, M. Galova, E. Schiebel, M. J.R.Stark, and K. Nasmyth, Cell **108(3)**, 317 (2002).

[55] S. L. Shaw, E. Yeh, P. Maddox, E. D. Salmon, and K. Bloom, J Cell Biol. **139(4)**, 985994 (1997).

[56] D. A. Lerit, J. T. Smyth, and N. M. Rusan, Chromosome Res. **21(3)**, 271286 (2013).

[57] G. Pereira, T. U.Tanaka, K. Nasmyth, and E. Schiebel, The EMBO Journal **20(22)**, 6359 (2001).

[58] M. Piel, P. Meyer, A. Khodjakov, C. L. Rieder, and M. Bornens, J Cell Biol. **149(2)**, 317 (2000).

[59] Y. M. Yamashita, A. P. Mahowald, J. R. Perlin, and M. T. Fuller, SCIENCE **315**, 518 (2007).

[60] I.-J. Lee, N. Wang, W. Hu, K. Schott, J. Bahler, J. Thomas H. Giddings, J. R. Pringle, L.-L. Du, and J.-Q. Wu, Mol Biol Cell **25(18)**, 27352749 (2014).

[61] C. Seybold and E. Schiebel, Current Biology **23(19)**, R858 (2013).

[62] G.Civelekoglu-Scholey, D.J.Sharp, A. Mogilner, and J. Scholey, Biophysical Journal **19(11)**,

3966 (2006).

[63] G. Fink, I. Schuchardt, J. Colombelli, E. Stelzer, and G. Steinberg, EMBO J. **25(20)**, 4897908 (2006).

[64] K. R. Finley, K. J. Bouchonville, A. Quick, and J. Berman, J Cell Sci **121**, 466 (2008).

[65] G. Letort, F. Nedelec, L. Blanchoin, and M. Thery, Mol Biol Cell **27(18)**, 283343 (2016).

[66] M. Dogterom and B. Yurke, Science **278(5339)**, 85660 (1997).

[67] V. Soppina, A. K. Rai, A. J. Ramaiya, P. Barak, and R. Mallik, Proc Natl Acad Sci USA **106(46)**, 193816 (2009).

[68] M. J. I. Muller, S. Klumpp, and R. Lipowsky, Proc Natl Acad Sci USA **105(12)**, 460914 (2008).

[69] S. M. Markus, K. M. Plevock, B. J. S. Germain, J. J. Punch, C. W. Meaden, and W. Lee, Cytoskeleton (Hoboken, NJ) **68(3)**, 15774 (2011).

[70] A. P. Joglekar and A. J. Hunt, Biophys J **83(1)**, 4258 (2002).

[71] S. Sau, S. Sutradhar, R. Paul, and P. Sinha, PLoS One **9(7)**, e101294 (2014).

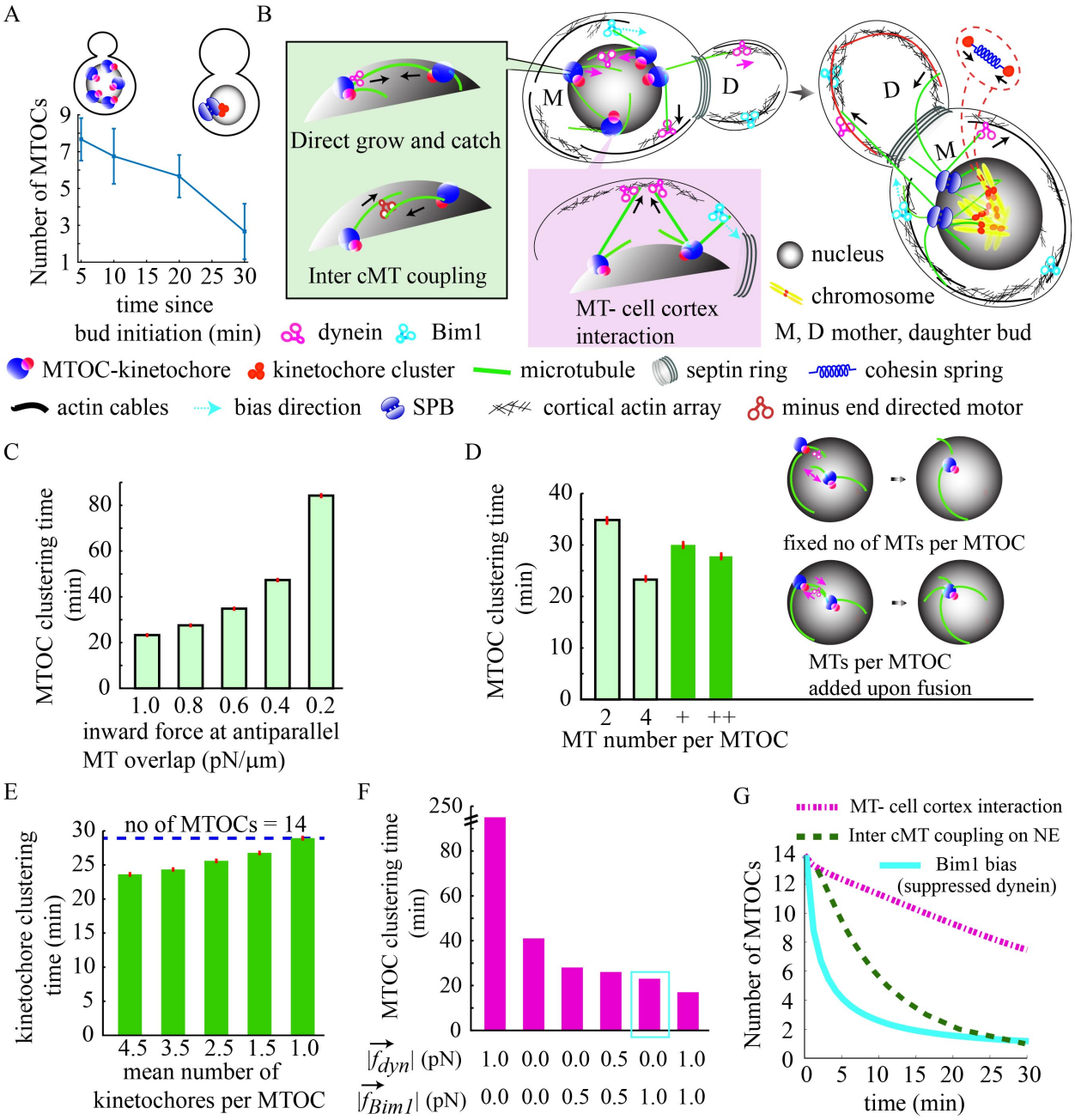

Figure 1. Cooperative interactions among MTs and motors govern MTOC clustering. (A) Number of MTOCs present in the cell as a function of time estimated from the bud size. (B) Model schematic depicting MT-mediated grow-and-catch ('search and capture') processes and various forces required for the clustering of MTOCs. Arrows indicate the direction of forces. Plausible clustering mechanisms illustrated here are: a growing cMT directly catching an MTOC ('direct grow-and-catch'), sliding of anti-parallel cMTs via crosslinking minus end-directed motors on the NE (inter cMT coupling at the NE)

and cMT plus-ends interacting with cell cortex (MT-cortex interaction). (C) Clustering time in the sole presence of inter cMT coupling at the NE increases as the minus ended motor generated inward force at MT-MT overlap decreases. The MT number is fixed at 4 per MTOC. (D) (First and second bars from left) MTOC clustering time with a fixed number of cMTs per MTOC. Clustering solely via 'inter cMT coupling at the NE' is considered here. (Third bar, +) Clustering time when every MTOC nucleates single cMT at the onset of the simulation and upon fusion the MTs of the fusing MTOCs aggregate up to a maximum of 4 cMTs per MTOC. (Fourth bar, ++) Similar to the "Third bar" but no constraint on the maximum number of cMTs per MTOC. (E) Asynchronous assembly of KTs/MTOCs, if more than one KT is associated with a single MTOC. (F) Clustering solely via MT-cell cortex interaction. The clustering is faster when Bim1 bias is enhanced. $|\vec{f}_{dyn}|$ ($|\vec{f}_{Bim1}|$) represents the magnitude of the force generated by single dynein (Bim1) on each MT at mother cortex. (G) Time progression of MTOC clustering in different mechanisms. The first/fifth bar in Figure 1F denote the parameter values corresponding to magenta/cyan curve in Figure 1G respectively. In all figures, sample size n>2000 for simulation and red bars indicate SEM (wherever shown).

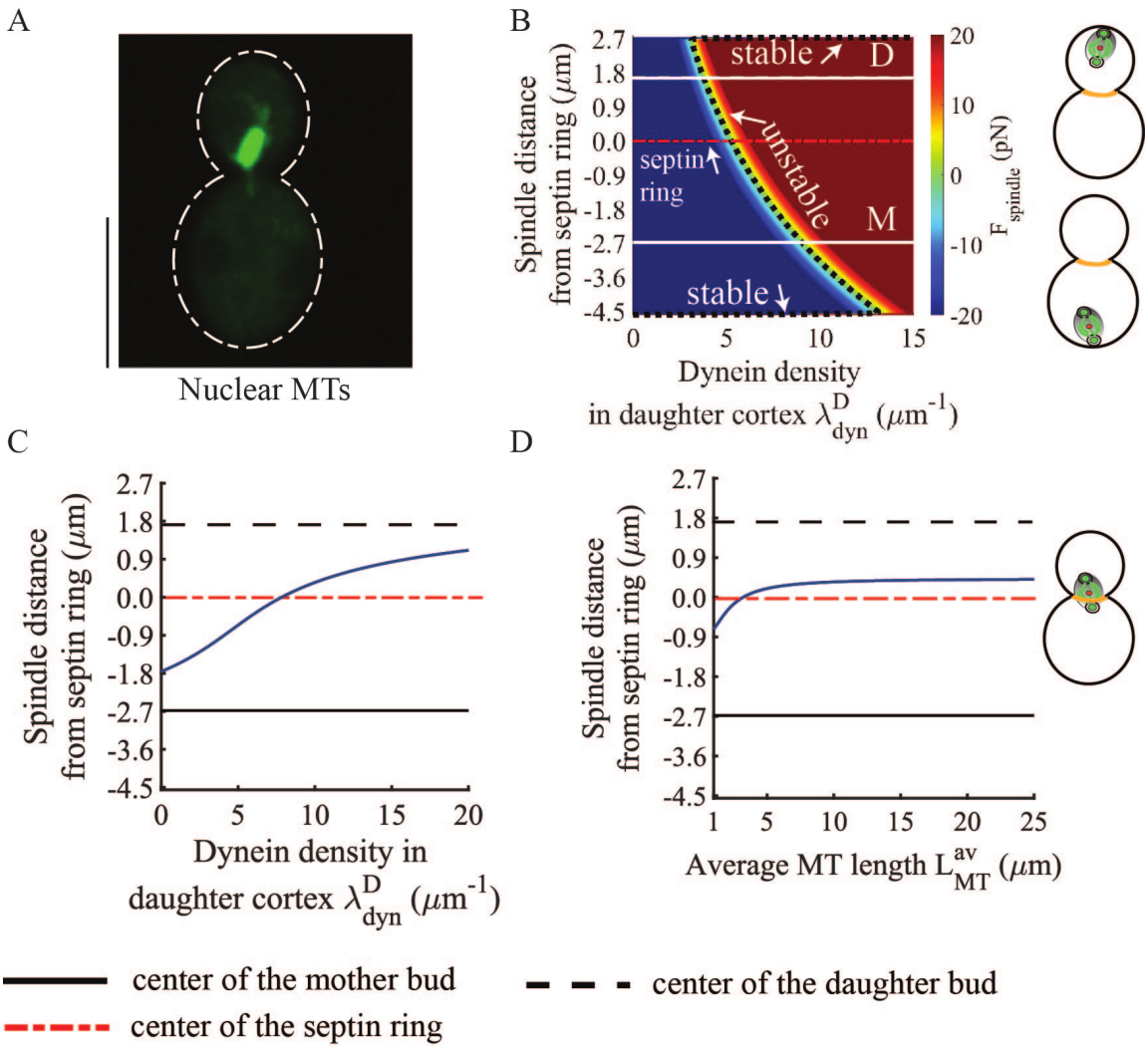

Figure 2. The mechanistic force balance model explains spindle positioning in *C. neorformans*. (A) Microscopic image of nMTs shows spindle position during anaphase in the wild-type cells expressing GFP-Tub1. Bar, 5 μm. (B) Spindle stably collapses onto the cell cortex as dynein density in the daughter cortex (λ^{D}_{dyn}) is varied. Dynein density in the mother cortex (λ^{M}_{dyn}) is fixed and instantaneous cortical push is present in both mother and daughter cortex. Colorbars represent the net force on the spindle and solid lines denote the center of the daughter and mother buds. (C) Step-wise increase in dynein density in the daughter cortex (λ^{D}_{dyn}) moves the spindle into the daughter cortex, localizing near the septin ring when MT buckling is combined with instantaneous push and dynein pull from the cell cortex. (D) Spindle position depending on the variation in average MT length (L^{av}_{MT}). Instantaneous cortical push, dynein pull, and MT buckling are present at both mother and daughter cortex. In plots B-D, -ve/+ve distance refers to the spindle in mother (M)/daughter (D) bud.

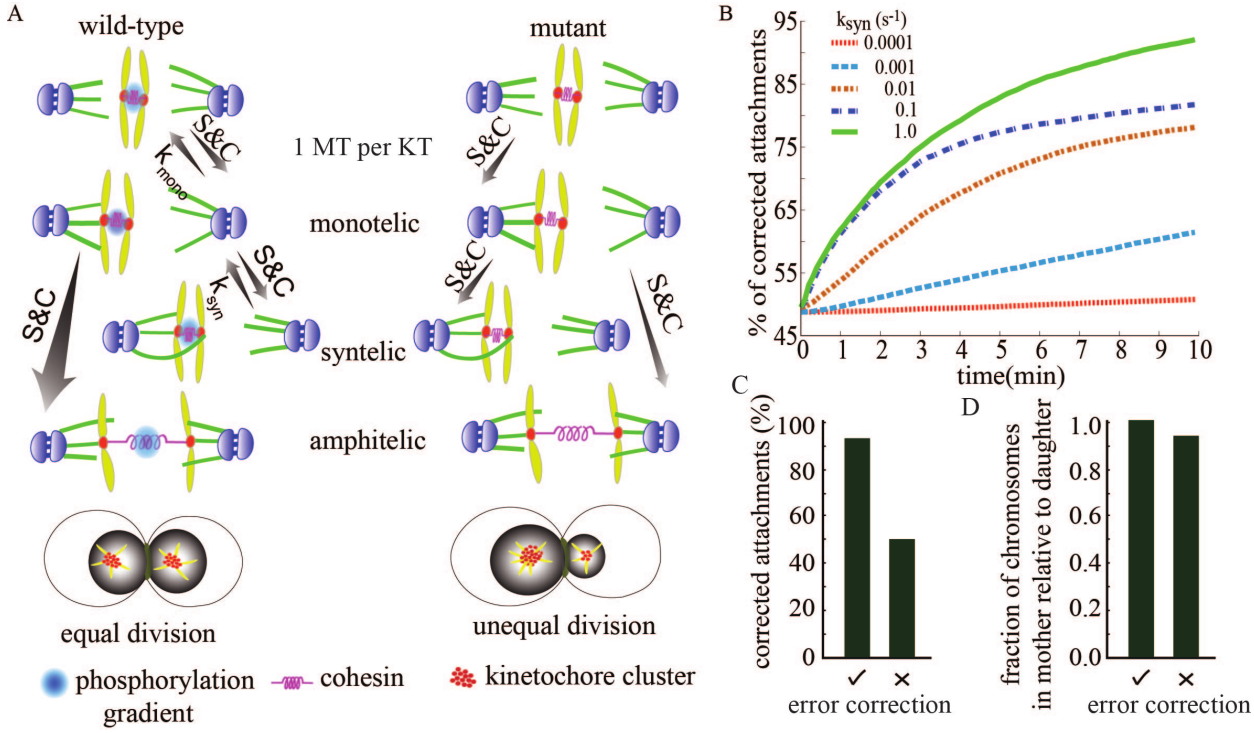

Figure 3. Correction of erroneous attachments and partitioning of chromosomes during division. (A) Schematic depicting possible kinetochore-MT attachments and corresponding chromosomal partitioning patterns. (left panel) Stable amphitelic configurations correlate with equal partitioning of chromosomes in wild-type, whereas (right panel) erroneous attachments (syntelic, monotelic) correlate with unequal partitioning. (B) The dynamics of error correction is correlated with syntelic degradation rate (k_{syn}). (C) Attachment statistics in the presence (absence) of correction mechanism. ✓/✗ represents the presence/absence of the mechanism. (D) The fraction of chromosomes in the mother relative to the daughter cell in the presence (absence) of correction mechanism.

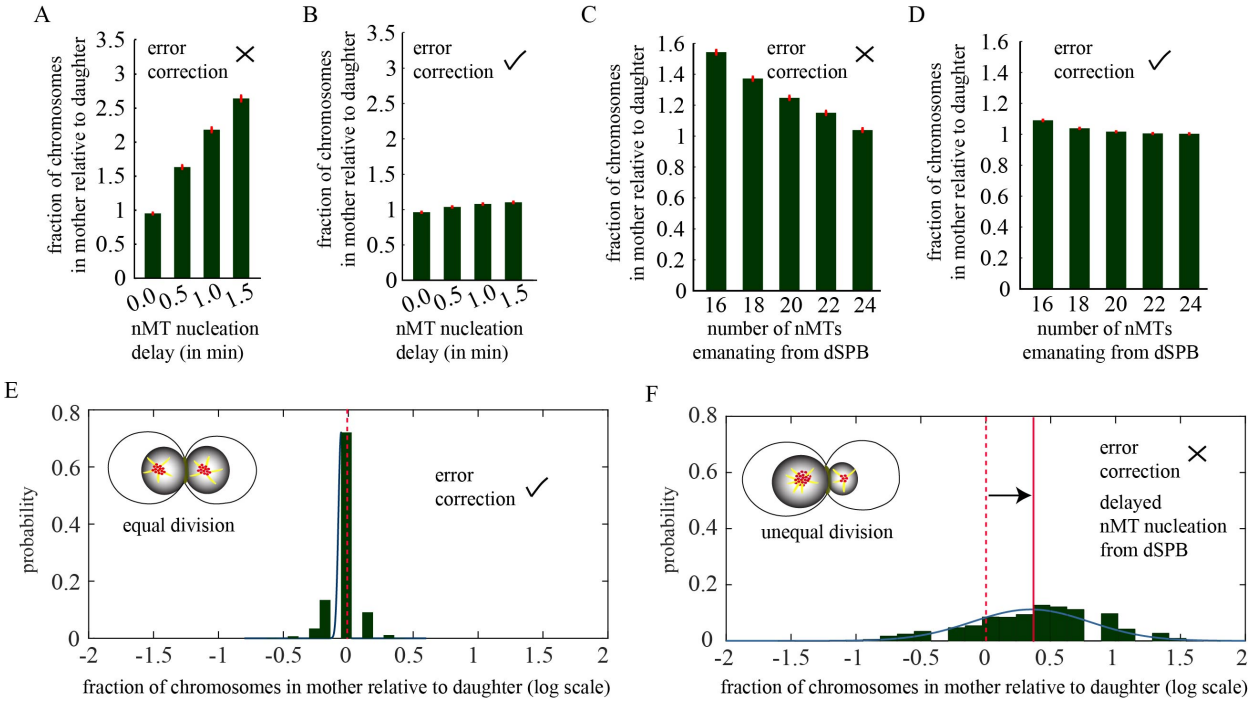

Figure 4. Impaired error correction mechanism together with MT nucleation defects lead to unequal division/aneuploidy. (A-B) Fraction of chromosomes in mother relative to daughter cell as the delay in MT nucleation from dSPB is varied in absence (A) or presence (B) of error correction. (C-D) Fraction of chromosomes in mother relative to daughter cell as nMT number nucleating from dSPB is varied in absence (C) or presence (D) of error correction. The number of nMTs from the mSPB is kept constant at 24. (E-F) Distribution of the fraction of chromosomes in mother relative to daughter cell in the wild-type and Ipl1 mutant in semi-log scale.